Three-dimensional printing of multicomponent glasses using phase-separating resins

David G. Moore[1,2], Lorenzo Barbera[1,2], Kunal Masania [ID][1]* and André R. Studart [ID][1]*

The digital fabrication of oxide glasses by three-dimensional (3D) printing represents a major paradigm shift in the way glasses are designed and manufactured, opening opportunities to explore functionalities inaccessible by current technologies. The few enticing examples of 3D printed glasses are limited in their chemical compositions and suffer from the low resolution achievable with particle-based or molten glass technologies. Here, we report a digital light-processing 3D printing platform that exploits the photopolymerization-induced phase separation of hybrid resins to create glass parts with complex shapes, high spatial resolutions and multi-oxide chemical compositions. Analogously to conventional porous glass fabrication methods, we exploit phase separation phenomena to fabricate complex glass parts displaying light-controlled multiscale porosity and dense multicomponent transparent glasses with arbitrary geometry using a desktop printer. Because most functional properties of glasses emerge from their transparency and multicomponent nature, this 3D printing platform may be useful for distinct technologies, sciences and arts.

Glass manufacturing dates back to Egyptian times and, ever since, has fascinated artists, scientists and technologists. From the invention of blowing in the ancient world to the spinning and manual rolling techniques widely used up to the nineteenth century, glass manufacturing has remained a highly empirical and laborious art[1]. Automation enabled by the first industrial revolution led to the mechanization of blowing and casting processes, setting new standards of productivity and quality. Process innovations in this industrialization phase played a remarkable role in glass technology, as exemplified by the Pilkington process for the fabrication of large flat windows[2] and the development of high-strength glasses for electronic displays (Gorilla Glass)[3]. Although automation and process innovations have increased the reproducibility, properties and quality of glass products, the symmetric and predominantly flat geometries achieved through these approaches remain remarkably limited compared to the intricate shapes that can be produced by manual artistic glass work.

The advent of three-dimensional (3D) printing technologies has opened enticing new possibilities for the manufacture of complex-shaped objects in a fully digital fabrication process. In the context of glasses, 3D printing can potentially reconcile the automation offered by modern industrial processes with even higher geometric complexity than is accessible by manual artistic labour. Recent developments in this direction have enabled 3D printing of single-phase, multicomponent glass objects by extrusion of the material in the molten state[4], direct writing of particle-based inks[5,6], laser-assisted filament melting[7] or stereolithographic patterning (SLA) of particle inks at room temperature[8,9]. These approaches offer distinct pathways, each with assets and drawbacks, towards the digital fabrication of glass. The 3D printing of molten soda-lime glass circumvents the high shrinkage and post-processing of conventional powder-based processes, but it requires melting of the feedstock material above 1,000 °C (see http://www.micron3dp.com). Direct ink writing of particle suspensions can lead to larger build sizes with moderate shrinkage, but suffers from the typical geometrical limitations of extrusion-based technologies[5,7]. Stereolithography using

particle-laden resins is a cost-effective alternative approach to achieve parts with higher geometric complexity compared to extrusion processes in applications that tolerate the high shrinkage associated with this technique[10–13]. However, the SLA-printed transparent glasses demonstrated so far have been based on SiO_2 nanoparticles, which limits the available chemistries. By contrast, examples of commercial glasses such as bioactive glass for bone regeneration, high-strength Gorilla Glass for displays and glass fibres for optical communications show that interesting functional properties often require compositions containing more than one oxide. Therefore, the development of technologies that broaden the compositional design space and improve the resolution of printed objects is key to advance this class of materials.

Higher printing resolutions can be achieved by using liquid molecular precursors instead of clustering-prone particle inks as feedstock resin for 3D printing. Liquid precursors have been successfully utilized to print ceramic parts with complex 3D geometries from pre-ceramic polymers[14–18]. In such systems, the ceramic phase is generated by pyrolysis of the molecular precursors under a reducing atmosphere at temperatures typically above 1,000 °C. However, this approach has been limited to SiO_2 and SiOC- and SiOCN-based compositions and related families of ceramics[15,18,19]. Broadening of the compositional design space towards other glass-forming oxides is potentially possible by using alkoxide precursors similar to those widely utilized in established sol–gel processes[20]. The potential of this approach is contingent upon the development of processing routes that minimize the distortion and defect formation normally associated with the removal of the reacted organic monomer phase that is required in photo-curing processes.

Here, we report a simple 3D printing process that relies on the phase separation of liquid resins to create complex-shaped glasses with high resolution and multi-oxide chemical compositions using a desktop digital light processing (DLP) printer. The resin primarily comprises alkoxide inorganic precursors, a photoactive monomer mixture and a light-absorbing dye (Fig. 1). Spinodal decomposition of the resin during photopolymerization generates a bicontinuous

[1]Complex Materials, Department of Materials, ETH Zurich, Zurich, Switzerland. [2]These authors contributed equally: David G. Moore, Lorenzo Barbera.
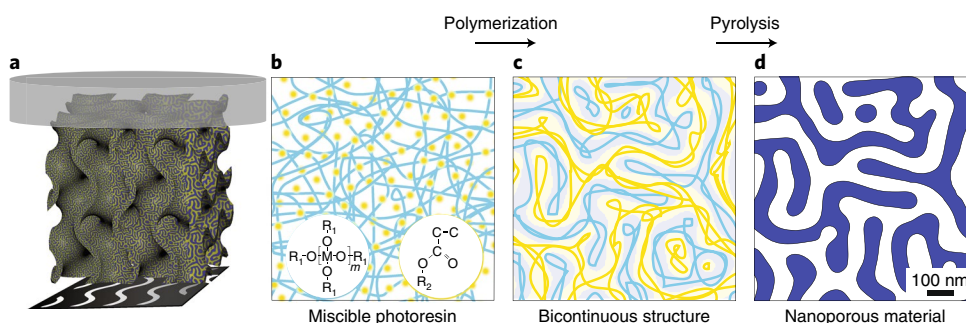*e-mail: kunal.masania@mat.ethz.ch; andre.studart@mat.ethz.ch

Fig. 1 | DLP 3D printing of phase-separating resins. a, Schematics of the process, illustrating the geometrical complexity generated by the illumination pattern and the nanostructure emerging from the phase separation phenomenon. **b,c**, In this process, acrylate monomers and pre-ceramic precursors such as poly(diethoxysiloxane) (PDEOS) are photopolymerized (**b**) to form a three-dimensionally defined bicontinuous structure of organic polymer and pre-ceramic polymer (**c**). **d**, The as-printed object is pyrolysed to form a nanoporous structure that can be optionally further sintered into transparent multi-material glasses and glass-ceramics.

morphology that is eventually arrested by the polymerization process[21]. By spatially controlling the grey-scale intensity of the digital light projection, the velocity of polymerization and thus the morphology of the bicontinuous phases can be tuned on the voxel scale. The enrichment of inorganic precursors into one of the phases enables the formation of porous structures with submicrometre pore sizes upon pyrolysis of the printed objects. Subsequent sintering of these porous bodies leads to transparent multicomponent glasses with complex geometries and precise spatially controllable chemical compositions. This process resembles the well-known Vycor technology, in which phase separation followed by etching is used to create a porous silica framework that can be fully densified into high-purity fused-silica glass at cost-effective processing temperatures[22]. In addition to locally controlling the pore size, phase separation plays two main roles in our fabrication process. First, it enables the formation of a continuous polymer network after printing that is strong enough to build mechanically stable 3D hybrid parts with truly complex geometries. Second, it allows for the development of an inorganic phase upon heat treatment of the as-printed part, which becomes sufficiently stable to withstand the pyrolysis process. Using inorganic precursors that result in multiple glass formers after pyrolysis allows us to 3D print glasses and glass-ceramics combining complex geometry, spatially controllable porosity and a broad multi-oxide compositional range into a single object.

We illustrate the proposed technology by first selecting a resin formulation that undergoes well-defined phase separation upon photopolymerization (Fig. 2). The selected formulation is an acrylate-based resin containing poly(diethoxysiloxane) (PDEOS), triethyl phosphate (TEP) and trimethyl borate (TMB) as molecular precursors for silicon, phosphorous and boron glass-forming oxides, respectively. A commercial urethane acrylate (UA, Neorad U25-20D) and tripropyleneglycol diacrylate (TPGDA) were used as multifunctional monomers. Acrylates are ideal monomers for this approach because they are (1) easily photopolymerized with free radical processes, (2) chemically compatible with all glass-forming oxide precursors and (3) can be thermally removed through depolymerization. Besides these core components, this exemplary resin also contains a light-absorbing dye (Sudan I) and a photoinitiator (diphenyl(2,4,6-trimethylbenzoyl)-phosphine oxide, TPO).

The phase behaviour of the resin is schematically depicted in a pseudo-quinary diagram displaying the miscibility gap for different concentrations of the five main components: PDEOS, TEP, TMB, TPGDA and UA (Fig. 2a). This diagram was experimentally determined from cloud point measurements in solutions containing pre-defined compositions before polymerization. The total amount of monomer (TPGDA and UA) defines one of the corners of the phase diagram, whereas the relative ratio of the monomers (% UA) is

indicated by iso-lines projected on a subset of ternary systems. The UA is highly immiscible with the alkoxide PDEOS and thus can be added to increase the size of the miscibility gap and promote phase separation of the resin. By contrast, the inorganic precursor TEP is miscible in both PDEOS and the monomer mixture. Therefore, increasing the TEP concentrations moves the system further from the miscibility gap and prevents phase separation. All compositions used in this work reside on the 40% monomer plane that was identified as the minimum amount of monomer necessary to achieve a bicontinuous phase-separated system (Fig. 2b).

Based on these general trends, we selected two resin compositions that are either close or far from the miscibility gap and qualitatively assessed the macroscopic appearance of objects printed with these different resins (Fig. 2c). Although these two compositions lie initially in the miscible region of the diagram, polymerization of the monomers should increase the size of the miscibility gap and thus induce the phase separation process during printing. The printed objects were fabricated in a gyroid geometry using a conventional DLP printer operating with a light-emitting diode (LED) light source at a wavelength of 405 nm. For SLA the exposure is controlled by the residence time of a constant-intensity laser, but DLP allows the light intensity to be programmed on the voxel scale by tuning the grey scale within projected layers. The resulting specimens present a significantly distinct visual appearance depending on the formulation used. For example, a resin with composition far from the miscibility gap led to a translucent object, with the same appearance as samples containing only the monomers (Fig. 2c). By contrast, a more opaque sample was obtained with the formulation closer to the immiscible region, indicating the presence in this case of a higher density of light-scattering interfaces with feature sizes comparable or larger than the wavelength of the light. These first results confirm the possibility of creating a bicontinuous network of inorganic-rich and polymer-rich phases through polymerization-induced phase separation, provided that the resin composition is sufficiently close to the miscibility gap in the phase diagram.

To better understand the dynamics of the phase separation process and its effect on the microstructure of the printed objects, we performed systematic experiments with resins of fixed composition printed under distinct greyscales of the desktop 3D printer to cover light intensities in the range 0.22–22 mW cm^{-2} (Fig. 3). The light intensity controls the velocity of the polymerization reaction, which, in turn, arrests the phase separation process. Because the characteristic domain size of the bicontinuous network created via spinodal decomposition increases with time, faster polymerization should lead to finer phase-separated morphologies.

The effect of light intensity on the phase-separated morphologies was studied using a resin formulation that is suitable for the
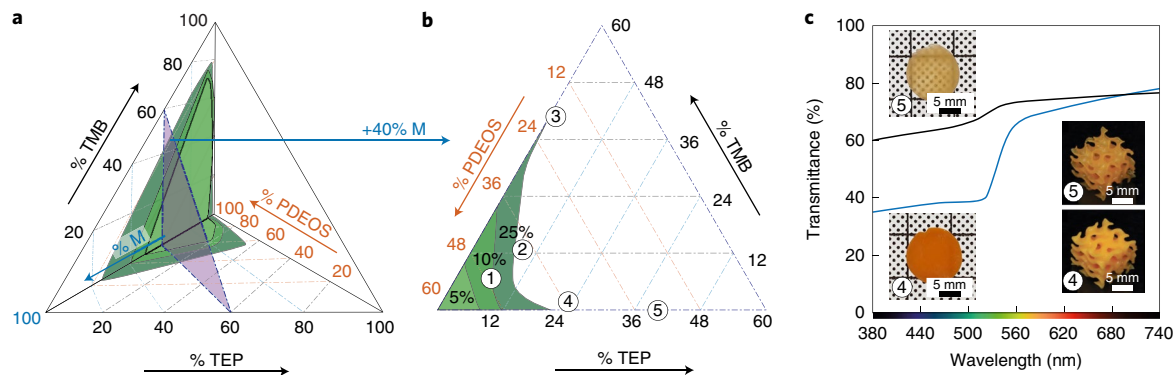
Fig. 2 | Resin composition determines the degree of phase separation during DLP printing. a, Pseudo-quinary phase diagram of exemplary resins containing PDEOS, TEP, TMB and the monomers TPGDA and UA. The monomer (M) concentration indicated in the diagram refers to the total monomer amount, given by $(1-x) \times TPGDA + x \times UA$, where x is the percentage of UA. The phase-separated regions are indicated as filled green areas on a subset of ternary diagrams. **b**, Ternary diagram obtained for a fixed monomer concentration of 40%, indicating all the compositions that were 3D-printed. **c**, Optical transmittance of 1.2-mm-thick samples prepared from two specific formulations. A composition with 22.3% TEP, labelled '4', is close to the immiscible region and becomes turbid after polymerization, thus indicating successful phase separation (blue curve). A composition with 39.9% TEP, labelled '5' remains transparent when polymerized because the formulation is far from the immiscible region of the phase diagram (black curve). The insets show the actual 3D printed parts obtained with these two compositions.
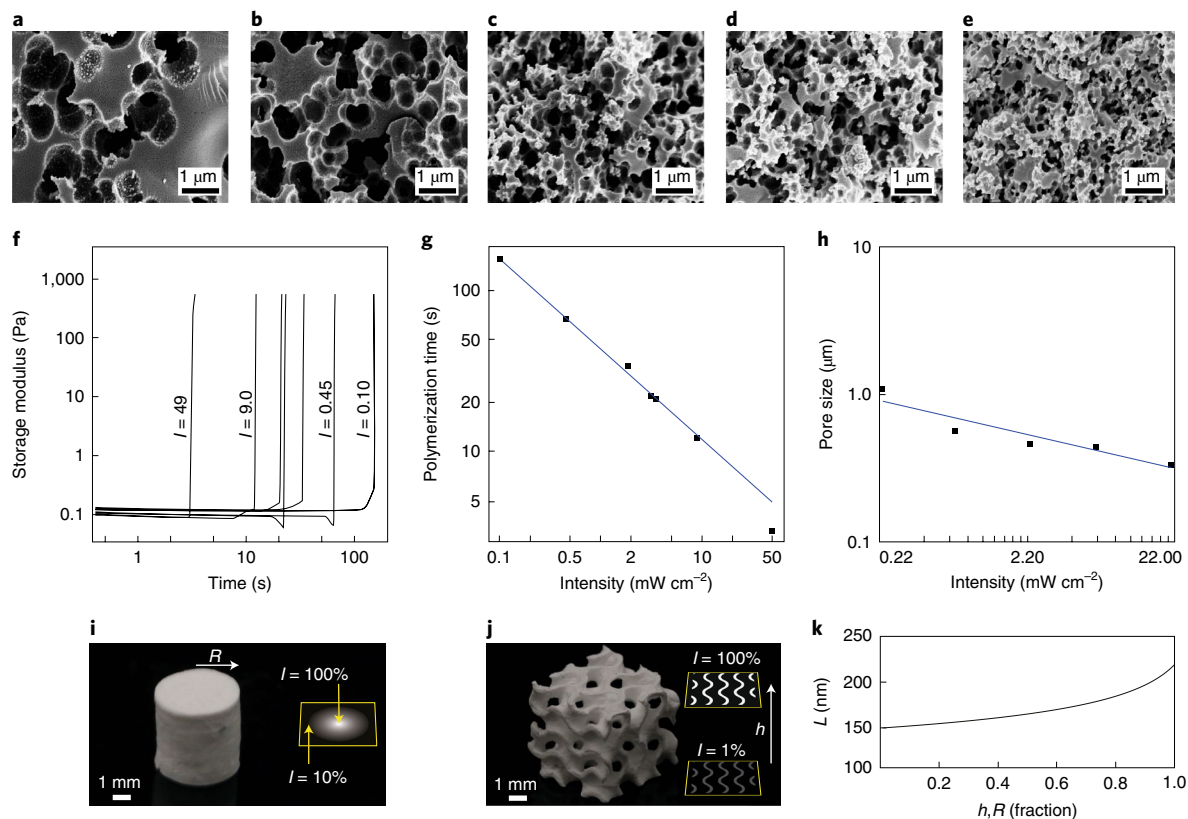

Fig. 3 | Light-controlled pore size in 3D printed glass objects. a–e, Scanning electron microscopy (SEM) images of porous ceramics obtained with light intensities of 0.22, 0.66, 2.20, 6.60 and 22.00 mW cm⁻² (from left to right). **f**, Evolution of the storage modulus of the resin upon illumination using different light intensities (in mW cm⁻²). **g**, Dependence of polymerization time t_{pol} on light intensity. The polymerization time corresponds to the timepoint at which the storage modulus of the resin sharply increases. **h**, The effect of the light intensity on the average pore size of the printed structures after pyrolysis. **i,j**, 3D printed glass objects featuring a programmed gradient in pore size along the radius R or height h of a cylinder (**i**) and of a gyroid (**j**) structure, respectively. **k**, The gradient is created by illuminating the resin with a light intensity profile that leads to a continuous change in strut and pore size as a function of radius (cylinder) or height (gyroid). These results were obtained using a resin with composition 2 from the phase diagram in Fig. 2b (Supplementary Table 1).

production of multicomponent glasses in the system SiO_2–B_2O_3–P_2O_5 (composition 2 in Fig. 2a,b). In such a formulation, PDEOS, TEP and TMB are the ceramic precursors used to obtain, respectively, silicon, phosphorous and boron oxides after pyrolysis and sintering. For microscopic analysis of the phase-separated morphologies, resins exposed to different light intensities during

printing were pyrolysed in an electric furnace at 700 °C using a constant heating rate of 0.4 °C min⁻¹. Thermogravimetric analysis (TGA) and differential thermal analysis (DTA) of the resin indicate that the condensation reaction of the metal alkoxides occurs in the temperature range 200–400 °C, whereas pyrolysis of the organic phase takes place between 350 and 400 °C (Supplementary Fig. 1). Although temperatures above 200 °C are required to promote the condensation reaction, we observed that the as-printed object undergoes an aging process if left at room temperature before the thermal treatment. This aging process probably results from an initial slow reaction of the alkoxides and is characterized by a linear shrinkage of the object of ~3.5% (Supplementary Fig. 2a). Pyrolysis leads to an additional linear shrinkage of the printed object of ~30%, as evidenced by direct measurements on a representative resin (Supplementary Fig. 2a). Because the thermally induced condensation of the metal alkoxides begins before pyrolysis of the organic phase, a continuous and self-supporting metal oxide network forms without the need for chemical crosslinkers. This defines the basis for the greater chemical versatility of our approach. Metal alkoxides may vary broadly in chemical reactivity towards acid and base catalysts or acrylation compounds, but virtually all begin to calcine below 350 °C.

Microstructural analysis of the heat-treated specimens showed that the removal of the polymer phase results in highly porous ceramics, with pore sizes and strut dimensions decreasing with increasing printing light intensities (Fig. 3a–e and Supplementary Fig. 3). We quantified the strut size distributions of graded porous structures using image analysis and found that light intensities of 0.22, 2.2 and 22 mW cm⁻² within a single printed object lead to porous morphologies with average strut dimensions of 320, 210 and 150 nm, respectively (Supplementary Fig. 3). Remarkably, we find that the light intensity variation within a single print layer is enough to create pore size gradients at length scales even below the layer thickness, if a high concentration of light-absorbing dye is used (Supplementary Fig. 4). This demonstrates that arresting the polymerization-induced phase separation by light is indeed an effective way to control the pore sizes of the printed inorganic structures.

The ability to tune the morphology of the polymerized resins with light opens the possibility of 3D printing materials with voxel-specific structure, composition and properties using the same feedstock resin. To further explore this idea and eventually implement this site-specific programmability in DLP printing, we established a direct quantitative correlation between the light intensity applied during manufacturing and the final feature size of the printed structures. Morphological characterization of samples that were polymerized over a broad range of light intensities show that the average strut size L follows a power-law dependence with the intensity I ($L \approx I^{-b}$, with $b = 0.18$; Supplementary Fig. 5). A similar power exponent is observed for the dependence of the average pore size on light intensity (Fig. 3h).

To understand the origin of this power-law dependence, a theoretical analysis of the phase separation process and additional experiments were performed. We hypothesize that the exponent b of the power law is determined by the dynamics of the spinodal decomposition that causes phase separation of the resin. The dynamics of spinodal decomposition can be quantitatively described by the Cahn–Hilliard equation, which predicts that the domain size of the phase-separating system coarsens over time (t) according to[23] $L \approx t^{1/3}$. Given that the elapsed time is controlled by the light-tunable polymerization kinetics, this equation can be used to describe the distinct observed morphologies if an explicit correlation between light intensity I and the timescale needed for polymerization (t_{pol}) is known.

The dependence of t_{pol} on I was assessed using oscillatory rheometry by measuring the time needed for the resin storage modulus to sharply increase under different illumination intensities (Fig. 3f). The rheological data show that the polymerization timescale can be described by another simple power relation, $t_{pol} \approx I^{-c}$. An exponent $c = 0.56$ was obtained by fitting this power law to our experimental data (Fig. 3g).

Assuming that the phase separation process is arrested at $t = t_{pol}$, the above relation can be introduced into the Cahn–Hilliard equation to extract a new power exponent b from our independent rheological measurements. An exponent b of 0.19 was obtained through this analysis, which is remarkably close to the value of 0.18 determined from our independent microstructural characterization. This provides strong evidence that the porous morphology of the printed resins is indeed controlled by the phase separation effect induced and arrested by the polymerization reaction.

The ability to program the morphology of oxides using light-induced phase separation was further exploited to DLP print hierarchical ceramics with complex macroscopic geometry and voxel-specific pore sizes at the nanoscale (Fig. 3i–k). In a first simple demonstration, a cylindrical object with a gradient in pore size along the radial direction was prepared by exposing the phase-separating resin to a radial light intensity profile at each individual print layer (Fig. 3i,k). Next, the concept was taken to another complexity level by 3D printing a macroscopic gyroid structure featuring a linear gradient in pore size along the vertical direction (Fig. 3j,k). In both examples, the objects showed good mechanical integrity after the pyrolysis process, in spite of the differential stresses expected in the structure during thermal degradation of the organic phase. Although the local pore size at the microstructural level is determined by the light intensity applied in the printing process, the porosity is controlled by the fraction of organic phase in the initial composition and the associated shrinkage of the object during the aging and pyrolysis steps. In addition to shrinkage, the build volume and the structural complexity are other relevant parameters in 3D printing processes. Although the build volumes accessible by DLP printing are typically smaller than those of direct writing approaches, the level of geometrical complexity demonstrated in the gyroid structure is a major feature that is not easily achieved with other techniques. Moreover, the creation of nanopores with deliberately controlled sizes within a macroscopic object provides a powerful means to fabricate complex structures with voxel-specific properties, such as effective thermal conductivity, refractive index and diffusion coefficients.

In addition to hierarchical porous materials, DLP 3D printing of phase-separating resins enables the fabrication of complex-shaped glasses with multi-oxide functional compositions. In this case, pyrolysed nanoporous objects are sintered at higher temperatures to fully densify the phase-separated morphologies (Fig. 4a). These glasses show high transparency with absorption cutoffs lower than 300 nm (Fig. 4b) and a glass transition temperature of 771 °C (Supplementary Fig. 1a). We illustrate this by using three exemplary resin compositions in the SiO_2–B_2O_3–P_2O_5 system. The compositions were chosen to demonstrate the broad range of chemistries covered by this process. The concentrations of the inorganic precursors were intentionally selected to lie close to the SiO_2–B_2O_3–P_2O_5 eutectic line to prevent crystallization and thus obtain glasses at moderate cooling rates[24] (Fig. 4c). During sintering of these compositions, we observed a linear shrinkage in the range of 23–26% based on the object dimensions after pyrolysis (Supplementary Fig. 2b). Considering all fabrication steps, the total linear shrinkage of the printed object typically falls within the 60% range (Supplementary Fig. 2a). Pycnometry measurements indicate a density of 2.18 g cm⁻³ for the glass object after sintering. Assuming a typical specific gravity of borosilicate glasses to be 2.23 g cm⁻³ (ASTM E438), this corresponds to a relative density of 98%.

Three-dimensional glass objects with high transparency were successfully printed and sintered in a wide range of complex geometries and multicomponent compositions (Fig. 4d). These printed objects were verified to be amorphous using X-ray diffraction
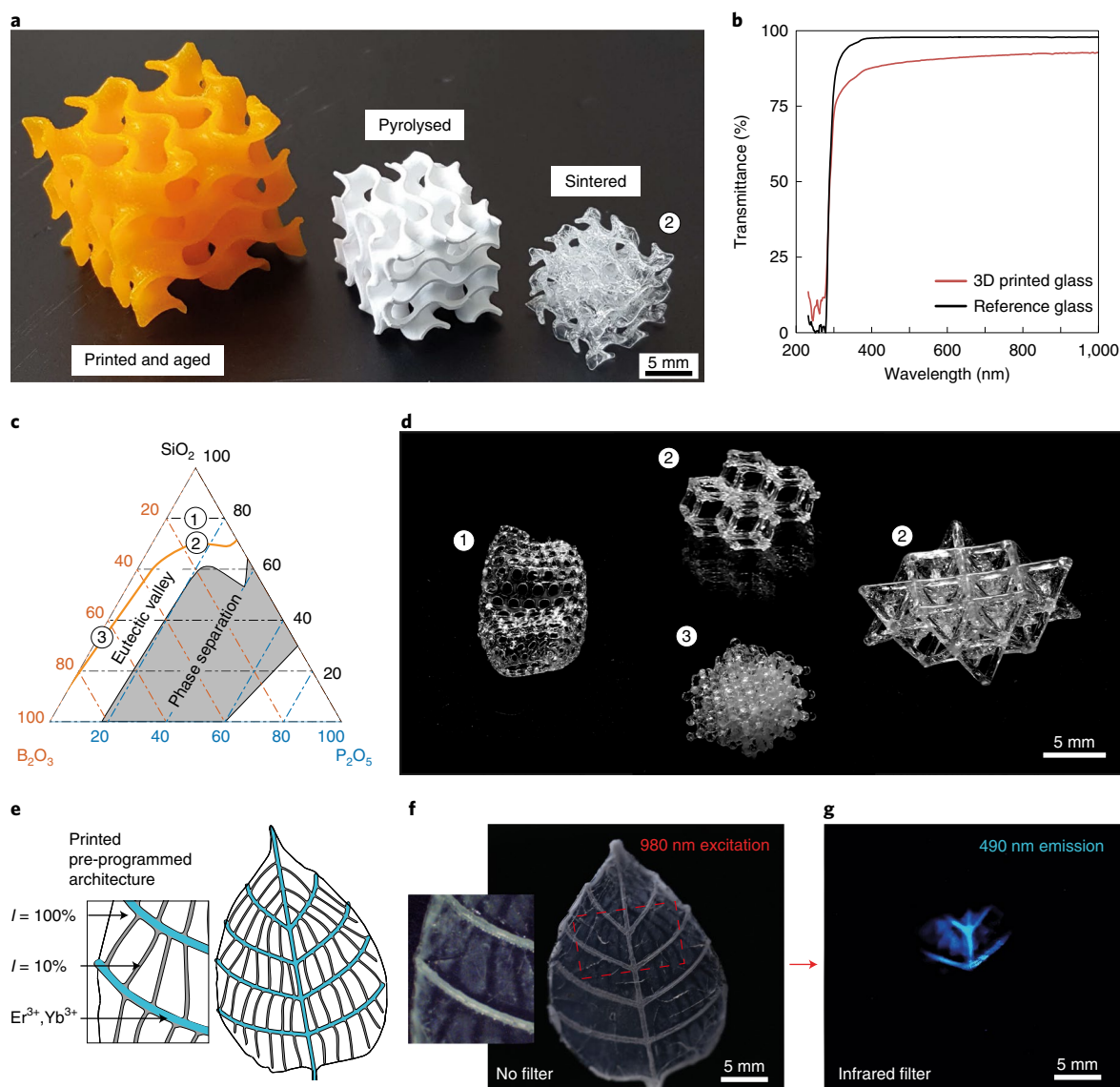
Fig. 4 | Boro-phospho-silicate (BPS) glasses obtained by 3D printing of phase-separating resins. a, Illustrative picture of a complex-shaped object along different stages of the process. **b**, Optical transmittance of the 3D printed glass in comparison to a highly transparent reference. **c**, Phase diagram of the BPS system indicating the glass compositions used to print the objects shown in this figure. **d**, Transparent and dense BPS glasses obtained by sintering 3D printed porous objects. High transparency is achieved by choosing compositions at or close to the eutectic valley, which results in homogeneous melting at high temperatures. **e–g**, Multi-material 3D printed glass exhibiting a complex leaf-like geometry. The main body of this exemplary leaf structure was printed using resin composition 2 from the phase diagram in **c**. In **e,f**, illumination of this resin with different intensities during printing led to distinct levels of transparency that create the pattern of primary and secondary veins. An erbium–ytterbium doped glass composition was printed on top of the main body along the primary veins of the leaf. When illuminated with infrared light (**g**), the areas covered with the doped glass show strong blue colour due to upconverted photoluminescence.

(Supplementary Fig. 6). We used our thermal gravimetric analysis (Supplementary Fig. 1) to evaluate whether the inorganic precursors evaporate during the heat treatment. Our results suggest that most of the inorganic precursors remain in the structure after pyrolysis, leading to a final glass composition that is close to that expected from the initial resin formulation (see Methods and Supplementary Table 1).

In a final demonstration of the potential of the proposed technology, we 3D printed a glass leaf with locally tunable optical properties by exploiting the voxel-specific control over the pore size and chemical composition of the object (Fig. 4e). The leaf was designed to display primary and secondary veins, forming a hierarchical bifurcated pattern throughout the 3D object. The pattern of secondary veins was created by exposing parts of the leaf to a light intensity of

2.20 mW cm^{-2}, while the remainder of the object was printed using 10-fold stronger illumination. Because of the different sinterability of the microstructures with distinct pore sizes, firing of the printed object led to a glass leaf with a bifurcated vein pattern comprising translucent regions separated by transparent secondary veins (Fig. 4f). Primary veins were printed on top of the object using a second resin composition containing lanthanide salts that feature photon upconversion properties. In this multi-material approach, the resins are exchanged during the printing process and the resulting 3D object is subjected to pyrolysis and sintering in a single heat treatment. The final glass leaf has a unique appearance when illuminated with a collimated beam of 980 nm infrared light. Photon upconversion at the lanthanide-containing voxels turns the incident infrared radiation into blue light, making the primary veins of the glass leaf stand

out colourfully in the otherwise transparent and translucent background pattern (Fig. 4g and Supplementary Fig. 7).

In summary, we show that DLP 3D printing of phase-separating resins is a unique platform for the digital fabrication of complex-shaped designer glasses with voxel-specific composition, structure and properties. The phase separation phenomenon at the heart of this process is both induced and arrested by the photopolymerization reaction of monomers present in the initial resin. This makes the process fully controllable by the light applied during printing, as exemplified by the tunable pore sizes achieved by simply varying the illumination intensity at specific voxels. Because polymerization-induced phase separation is a universal physical process, we envision this technology to be also applicable to a broad range of chemical compositions and additive processes (for example, ink jet). In analogy to the well-established sol–gel chemistry, a rich variety of inorganic precursors can be potentially structured into porous or dense glasses and glass-ceramics using this additive manufacturing technique. With the high-resolution complex geometries and locally tunable structure of the multicomponent glasses demonstrated in this work, the proposed 3D printing platform is a step towards combining the high level of automation offered by modern digital fabrication processes with the accurate control over shape and chemistry traditionally achieved by manual labour.

Online content

Any methods, additional references, Nature Research reporting summaries, source data, extended data, supplementary information, acknowledgements, peer review information; details of author contributions and competing interests; and statements of data and code availability are available at https://doi.org/10.1038/s41563-019-0525-y.

References

1. Pfaender, H. G. *Schott Guide to Glass* (Springer, 2012).
2. Pilkington, L. A. B. Review lecture: the float glass process. *Proc. R. Soc. Lond. A* **314**, 1–25 (1969).
3. Hale, D. Strengthening of silicate glasses by ion exchange. *Nature* **217**, 1115 (1968).
4. Klein, J. et al. Additive manufacturing of optically transparent glass. *3D Print. Addit. Manuf.* **2**, 92–105 (2015).
5. Nguyen, D. T. et al. 3D-printed transparent glass. *Adv. Mater.* **29**, 1701181 (2017).
6. Destino, J. F. et al. 3D printed optical quality silica and silica–titania glasses from sol–gel feedstocks. *Adv. Mater. Technol.* **3**, 1700323 (2018).
7. Luo, J. et al. Additive manufacturing of transparent soda-lime glass using a filament-fed process. *J. Manuf. Sci. Eng.* **139**, 061006 (2017).
8. Kotz, F. et al. Three-dimensional printing of transparent fused silica glass. *Nature* **544**, 337–339 (2017).
9. Liu, C., Qian, B., Ni, R., Liu, X. & Qiu, J. 3D printing of multicolor luminescent glass. *RSC Adv.* **8**, 31564–31567 (2018).
10. Bártolo, P. J. *Stereolithography: Materials, Processes and Applications* (Springer, 2011).
11. Wong, K. V. & Hernandez, A. A review of additive manufacturing. *ISRN Mech. Eng.* **2012**, 208760 (2012).
12. Wu, C., Luo, Y., Cuniberti, G., Xiao, Y. & Gelinsky, M. Three-dimensional printing of hierarchical and tough mesoporous bioactive glass scaffolds with a controllable pore architecture, excellent mechanical strength and mineralization ability. *Acta Biomater.* **7**, 2644–2650 (2011).
13. Tesavibul, P. et al. Processing of 45S5 Bioglass® by lithography-based additive manufacturing. *Mater. Lett.* **74**, 81–84 (2012).
14. Zocca, A. et al. SiOC ceramics with ordered porosity by 3D-printing of a preceramic polymer. *J. Mater. Res.* **28**, 2243–2252 (2013).
15. Eckel, Z. C. et al. Additive manufacturing of polymer-derived ceramics. *Science* **351**, 58–62 (2016).
16. Zanchetta, E. et al. Stereolithography of SiOC ceramic microcomponents. *Adv. Mater.* **28**, 370–376 (2016).
17. Schmidt, J. & Colombo, P. Digital light processing of ceramic components from polysiloxanes. *J. Eur. Ceram. Soc.* **38**, 57–66 (2018).
18. Brinckmann, S. A. et al. Stereolithography of SiOC polymer-derived ceramics filled with SiC micronwhiskers. *Adv. Eng. Mater.* **20**, 1800593 (2018).
19. Cooperstein, I., Shukrun, E., Press, O., Kamyshny, A. & Magdassi, S. Additive manufacturing of transparent silica glass from solutions. *ACS Appl. Mater. Interfaces* **10**, 18879–18885 (2018).
20. Sanchez, C., Julián, B., Belleville, P. & Popall, M. Applications of hybrid organic–inorganic nanocomposites. *J. Mater. Chem.* **15**, 3559–3592 (2005).
21. Nakanishi, K. & Soga, N. Phase separation in silica sol–gel system containing polyacrylic acid. I. Gel formation behavior and effect of solvent composition. *J. Non-Cryst. Solids* **139**, 1–13 (1992).
22. Rabinovich, E. Preparation of glass by sintering. *J. Mater. Sci.* **20**, 4259–4297 (1985).
23. Zhu, J., Chen, L. Q., Shen, J. & Tikare, V. Coarsening kinetics from a variable-mobility Cahn–Hilliard equation: application of a semi-implicit Fourier spectral method. *Phys. Rev. E* **60**, 3564–3572 (1999).
24. Baret, G., Madar, R. & Bernard, C. Silica-based oxide systems. I. Experimental and calculated phase equilibria in silicon, boron, phosphorus, germanium and arsenic oxide mixtures. *J. Electrochem. Soc.* **138**, 2830–2835 (1991).

Methods

3D printing of phase-separating molecular resins. Resin compositions were defined by the wt% of their components. All chemicals were purchased from Sigma-Aldrich and used as provided unless otherwise noted. TEP, TMB and PDEOS were reagent grade and stored in a humidity-controlled cabinet. PDEOS was supplied by ABCR and was 48–52 equiv. wt% SiO_2. Acrylate monomers Neorad U25-20D (DSM Coating Resins) and TPGDA were used with polymerization inhibitor 4-methoxyphenol (MEHQ) as this plays an essential role in the oxygen inhibition necessary for DLP printing. A blue light-absorbing dye, Sudan I, was added at 0.005 wt% relative to the total resin content to achieve reasonable vertical resolution. TPO was added at 1.0 wt% of the total resin content. The compositions of resins 1–5 are listed in Supplementary Table 1. The resulting resins had a viscosity comparable to that of water and were used directly after mixing.

A commercial DLP 3D printer (Autodesk Ember) was used to program and fabricate the complex shaped structures from the phase-separating resins. The intensity of the light was programmed on a per-pixel basis by modifying the greyscale level from 1 to 100% of the slice images in the print file. The illumination intensities were calibrated using a G&R Labs Model 222 light meter and the full range of greyscale intensity was determined to correspond linearly to 0–22 mW cm^{-2}. The exposure dose was held constant at 48.4 mJ cm^{-2} for any given exposure, so the exposure time for 100% illuminated regions was 2.2 s and for 1% illumination regions was 220 s. To prevent sticking to the polydimethylsiloxane print surface, an adhesive fluorinated ethylene propylene film (McMaster Carr) was applied.

Phase diagrams of phase-separating resins. A pseudo-quinary phase diagram was constructed using the cloud point method[25]. Mixtures containing known amounts of resin components were titrated dropwise until a transition between transparency and turbidity was observed. The total sample volumes upon observation of the transitions were between 2 and 5 ml of solution. The phase diagrams were prepared according to the wt% of the constituents using the R package *ggtern*.

Condensation, pyrolysis and sintering of polymerized samples. The transformation of the phase-separated polymerized material to glasses includes the distinct processes of hydrolysis/condensation of the alkoxide precursors, pyrolysis of the acrylate polymer and possibly sintering of the porous oxide structure. To investigate these processes, TGA, DTA and mass spectrometry were performed in air (Supplementary Fig. 1). A large drop in weight over the temperature range 350–440 °C was observed using TGA. This was followed by a more gradual weight loss between 440 and 600 °C. Correspondingly, DTA showed two exothermic peaks with minima at 420 °C and 530 °C. The emitted materials were probably carbonaceous compounds and water. In-line mass spectroscopy recorded ions with mass-to-charge ratios of 18, 27 and 44, which are likely to correspond to the following compounds: H_2O^+ for $m/z = 18$; BO^+ or CH_2CH^+ for $m/z = 27$; CO_2^+ or $CH_2CH_2O^+$ for $m/z = 44$. A second set of emission peaks occurred at ~900 °C. These probably correspond to water and carbonaceous material trapped within the silica structure. As soon as the temperature exceeded the system glass transition temperature, the material had sufficient mobility to diffuse out of the sample.

The small peak at $m/z = 27$ revealed by mass spectrometry might be associated with a boron-containing species that evaporates from the structure during heat treatment. Because this peak coincides with that of a short hydrocarbon ionized molecule, it is not possible to draw a conclusion from this experiment alone. To evaluate the possibility of evaporation of this boron-containing species, we compare the measured and estimated total weight loss of the sample during pyrolysis. Assuming complete hydrolysis and condensation of the alkoxide precursors, the total weight loss expected if the inorganic phase does not evaporate from the structure is 78.2%. If the borate and phosphate were to evaporate and leave a silica-pure composition, this value would be 86%. Our TGA experiments on freshly printed samples show a total mass loss of 80%, suggesting that more than 90% of the glass precursors remain in the structure during pyrolysis and that the glass composition after heat treatment is close to that expected from the initial formulation.

From these analyses, a heat treatment protocol for condensation and pyrolysis was established. All heating steps were performed with a heating rate of 0.40 °C min^{-1} in a Nabertherm LT furnace. During the heat cycle, holds were performed at 500 °C for 6 h and at 700 °C for 4 h to promote diffusion of trapped organic materials and water. Debound samples, printed as cylinders with height of 5 mm and diameter of 5 mm, were sintered in a TA Instruments DIL 806 dilatometer to determine the sintering temperature. Samples 3D printed with uniform illumination intensities of $I = 1\%$, 10% and 100% were found to exhibit peaks in densification rate at 871, 893 and 927 °C, respectively (Supplementary Fig. 2b). To prepare transparent glass samples, debound samples were further heated to 1,000 °C and held for 4 h. Finally, samples were cooled to room temperature at a rate of 1 °C min^{-1} with a holding time of 12 h at 500 °C to relax internal stresses caused by densification.

The composition of resin 2 is near the phase-separating region of the B_2O_3–P_2O_5–SiO_2 phase diagram. Therefore, long holds of this composition at sintering temperatures may result in crystallization. However, X-ray powder diffraction confirmed the amorphous structure of the sintered samples

(Supplementary Fig. 6). Diffraction analysis was performed using an XPERT-PRO diffractometer equipped with a Spinner PW3064 sample stage and was integrated over a total of 5 h.

SEM sample preparation and strut thickness mapping. To measure the strut size distribution created from the phase separation process (Supplementary Fig. 3), a single sample was printed with a gradient in light intensity from 0.22 to 22 mW cm^{-2}, and afterwards pyrolysed as outlined above. Next, the sample was embedded in Epofix resin and sawed using a diamond tool to achieve a flat cross-section. After polishing using a Hitachi IM4000 broad ion beam, the sample was observed using a Zeiss LSM 510 electron microscope in backscatter detection mode using 10 kV acceleration voltage. In this contrast mode, the metal oxide appears white, whereas the epoxy-infiltrated region appears black. Strut size mapping was conducted using the 'Local thickness' plug-in for ImageJ[26]. The histograms for strut sizes in Supplementary Fig. 3g–i consist of the pixel counts for a given thickness summed over five separate images. In Supplementary Fig. 3d–f, the local thickness is plotted normalized to the maximum thickness in that image.

Photo-rheological measurements. The change in the storage modulus of the resin during photopolymerization was measured using an Anton Paar MCR 302 rheometer. The rheometer was equipped with a 43 mm diameter glass parallel-plate apparatus and set to a gap distance of 0.5 mm. A set of five 405 nm LEDs were mounted above the glass plate and connected in parallel to a power supply. A relationship between power supplied and illumination intensity was previously determined using a G&R Labs Model 222 light meter. Oscillatory measurements at 100 Hz with constant amplitude of 0.1% were acquired in synchronization with the 405 nm illumination.

Upconversion of Er^{3+}/Yb^{3+} doped glass. Upconversion was demonstrated by illuminating the sample with a 1.6 W 980 nm laser. The collimated light produced a rectangular projection of 5 × 8 mm on the sample. The photograph in Fig. 4g was taken with a conventional digital camera equipped with a 67 mm UV-IR cut filter (Haida Slim Pro-II). The upconversion process consists of a two-photon process in the erbium ion, where ytterbium plays the role of sensitizer (Supplementary Fig. 7).

Data availability

The datasets generated during and/or analysed during the current study are available from the corresponding authors on reasonable request.

Code availability

The *.stl and encoded microstructure print files are available from the corresponding authors on reasonable request.

References

25. Klenin, V. J. & Shmakov, S. L. Features of phase separation in polymeric systems: cloud-point curves (discussion). *Univers. J. Mater. Sci.* **1**, 39–45 (2013).
26. Dougherty, R. & Kunzelmann, K.-H. Computing local thickness of 3D structures with ImageJ. *Microsc. Microanal.* **13**, 1678–1679 (2007).

Acknowledgements

Author contributions

D.G.M., L.B., K.M. and A.R.S. conceived the idea together and designed the experiments. For the experimental work, D.G.M. focused more on the alkoxide chemistry, L.B. developed the sintering procedure and K.M. programmed the 3D printing microstructure. All the remaining experimental work was carried out by D.G.M., L.B. and K.M. D.G.M., L.B., K.M. and A.R.S. conducted the analysis and co-wrote the paper. All authors discussed the results and their implications, and revised the manuscript at all stages.

Competing interests

The authors have filed patent application EP18191209.8 related to this work.

Additional information

Supplementary information is available for this paper at https://doi.org/10.1038/s41563-019-0525-y.

Correspondence and requests for materials should be addressed to K.M. or A.R.S.

Reprints and permissions information is available at www.nature.com/reprints.